Spin disorder in a stacking polytype of a layered magnet

Xianghan Xu[1,*] Guangming Cheng,[2] Danrui Ni,[1] Xin Gui,[3] Weiwei Xie,[4] Nan Yao,[2] and R. J. Cava[1,*]
[1]*Department of Chemistry, Princeton University, Princeton, New Jersey 08544, USA*
[2]*Princeton Institute for the Science and Technology of Materials, Princeton University, Princeton, New Jersey 08544, USA*
[3]*Department of Chemistry, University of Pittsburgh, Pittsburgh, Pennsylvania 15260, USA*
[4]*Department of Chemistry, Michigan State University, Lansing, Michigan 48824, USA*

(Received 14 November 2022; revised 4 January 2023; accepted 1 February 2023; published 16 February 2023)

Strongly correlated ground states and exotic quasiparticle excitations in low-dimensional systems are central research topics in the solid-state research community. The present work develops a layered material and explores the physical properties. Single crystals of $3R$-Na_2MnTeO_6 were synthesized via a flux method. Single-crystal x-ray diffraction and transmission electron microscopy reveal a crystal structure with ABC-type stacking and an R-3 space group, which establishes this material as a stacking polytype to previously reported $2H$-Na_2MnTeO_6. Magnetic- and heat-capacity measurements demonstrate dominant antiferromagnetic interactions, the absence of long-range magnetic order down to 0.5 K, and field-dependent short-range magnetic correlations. A structural transition at ~23 K observed in dielectric measurements may be related to displacements of the Na positions. Our results demonstrate that $3R$-Na_2MnTeO_6 displays low-dimensional magnetism, disordered structure and spins, and the system displays a rich structure variety.

DOI: 10.1103/PhysRevMaterials.7.024407

I. INTRODUCTION

Low-dimensional magnetic systems have attracted research interest in recent years due to their potential for exhibiting spin entanglement and magnetic quantum states. For 1D or 2D Heisenberg spins, the ground state can be prevented from attaining long-range ordering at finite temperature, as proposed by the Mermin-Wagner theorem [1]. Long-range ordering can also be suppressed for Ising spins, through geometric frustration, leading to an entangled ground state [2,3]. Nevertheless, in the bulk crystals of many layered frustrated magnets, disorder or non-negligible interlayer exchange interactions often introduce spin freezing or long-range ordering in spite of expectations for layered systems [4–8].

The crystallographic symmetry of layered materials strongly depends on the stacking type of the atom layers. In the closest packing case, "AB" stacking results in a hexagonal cell ($2H$), while "ABC" stacking produces a rhombohedral cell ($3R$) [9]. Other types of stacking also create polytypes, such as seen for trigonal ($1T$) and monoclinic ($1T'$) $TaSe_2$ [10]. Different stacking types can play an important role in the electronic properties of layered materials as well. For instance, the $2H$ phase of $MoTe_2$ is semiconducting while the $1T'$ phase is semimetallic [11]. In the Kitaev spin-liquid candidate α-$RuCl_3$, stacking faults are believed to cause an anomalous magnetodielectric response [12]. Recently, ABC-stacked rhombohedral trilayer graphene has been found to exhibit superconductivity without being twisted [13], which is not the case for other stacking variants.

Despite the above-mentioned novel physics stemming from differences in stacking type, the interplay between stacking type and magnetism in layered magnetic insulators has not been well studied. This is partially due to the lack of magnetic layered-oxide materials that display stacking polytypes. The A_2MTeO_6 (A = Li, Na and M = Ti, Mn, Sn, Ge) family contains stacked 2D honeycomb structure units [14,15]. Na_2GeTeO_6 exhibits both $2H$ and $3R$ polytypes, suggesting that this layered-oxide family can display structural stacking variability. Recently, a magnetic compound, $2H$-Na_2MnTeO_6, has been described, with a commensurate 120° helical order found below 5.5 K [16]. However, the synthesis of the $3R$ version of Na_2MnTeO_6 in single-phase form has been argued to be infeasible [17]. Therefore, the synthesis of magnetic $3R$ compounds in this family is important but not reported to date.

Here, we experimentally demonstrate that the ABC-stacking type of a honeycomb layered magnet Na_2MnTeO_6 leads to an R-3 lattice ($3R$) as well as magnetism that is distinct from the previously reported hexagonal AB stacking ($2H$) compound with the same chemical formula. Single crystals of $3R$-Na_2MnTeO_6 are grown using a flux method. Magnetic- and heat-capacity study reveals a highly correlated ground state but no long-range magnetic ordering. Single-crystal x-ray- and electron-diffraction studies find a disordered distribution of Mn^{4+} and Te^{6+} ions in the honeycomb layer of the R-3 lattice. Magnetic measurements rule out long-range ordering down to 1.8 K. Heat-capacity measurements confirm the absence of long-range order down to 0.5 K and unveil the presence of field-dependent short-range correlations. Thus, we argue that $3R$-Na_2MnTeO_6 provides a high-quality platform for studying the magnetic excitation continuum in low dimension and

*xx8060@princeton.edu

the interplay between intersite disorder and spin-disordered states.

II. EXPERIMENT

Single crystal of 3*R*-Na_2MnTeO_6 was grown by a flux method. Na_2CO_3 (99.5%, Alfa Aesar), Mn_2O_3 (98%, Alfa Aesar), and TeO_2 (99.99%, Alfa Aesar) powders in molar ratio 6:1:12 were mixed, placed in a platinum crucible, heated to 850 °C in air, soaked at that temperature for 10 h, cooled to 500 °C at 3 °C/h, and then cooled at 100 °C/h to room temperature. The 3*R*-Na_2MnTeO_6 crystals with hexagonal plate shape and typical size 3 mm × 3 mm × 50 μm were mechanically separated after bathing the product in a 1M NaOH water solution overnight. Similar flux-growth method was used to grow 3*R*-Li_2GeTeO_6 crystals with a slower cooling rate [18].

Single-crystal diffraction was performed in a Bruker single-crystal x-ray diffractometer. The refinement was performed by using the SHELXTL software package [19,20]. Scanning electron microscopy (SEM) images were collected using a Quanta 200 FEG Environmental-SEM. Thin lamellae were prepared for TEM study by focused ion-beam (FIB) cutting using a Helios NanoLab G3 UC dual-beam FIB/SEM system. Sample thinning was accomplished by gently polishing the sample using a 2-kV gallium ion beam in order to minimize surface damage caused by the high-energy focused ion beam. Conventional TEM imaging, selected area eectron diffraction (SAED), atomic-resolution high-angle annular dark-field scanning transmission electron microscopy (HAADF-STEM) imaging, and energy-dispersive x-ray spectroscopy (EDS) mapping were performed on a Titan Cubed Themis 300 double Cs-corrected scanning transmission electron microscope (STEM) equipped with an extreme field-emission gun source operated at 300 kV with a super-X EDS system. The system was operated at 300 kV.

The temperature-dependent magnetization and heat-capacity measurements were performed in a Quantum Design PPMS-9 Dynacool. A Hellium-3 refrigerator was used to collect the heat-capacity data below 2 K. The dielectric permittivity was measured using a QuadTech 7600 LCR meter externally connected to the physical property measurement system (PPMS) probe. The electrodes were made of silver epoxy.

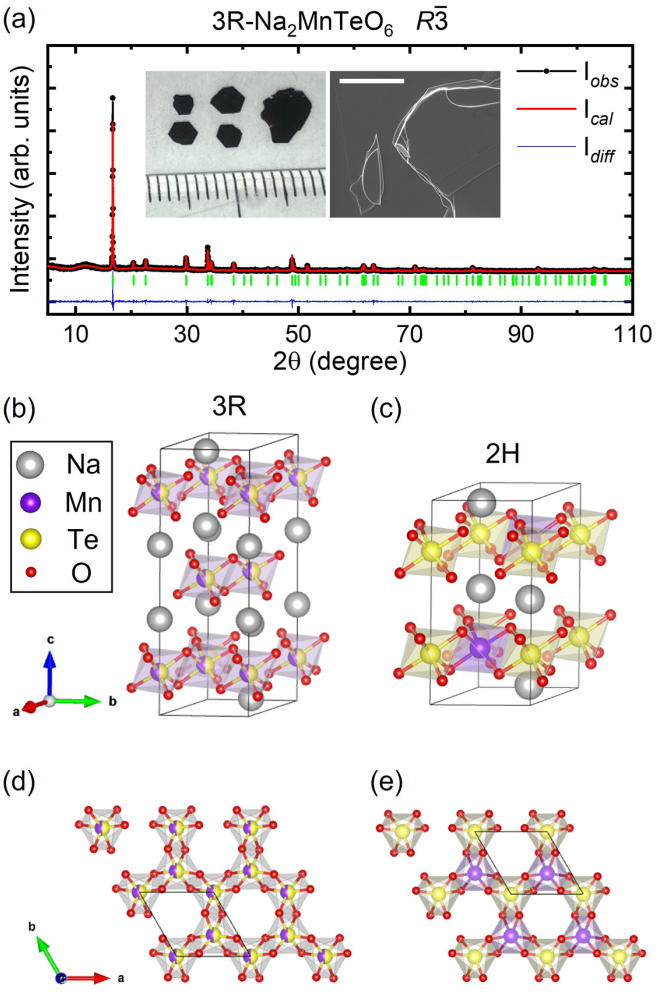

FIG. 1. (a) The black curve displays the powder XRD collected on the ground powder of 3*R*-Na_2MnTeO_6 crystals. The Le Bail fitting and the difference curves are shown in red and blue, respectively. Green bars exhibit Bragg peak positions. The inset displays a photograph of as-grown 3*R*-Na_2MnTeO_6 single crystals and an SEM image taken on the cleaved surface. The white scale bar is 40 μm. (b), (c) Crystal structures of 3*R*- (b) and 2*H*- (c) Na_2MnTeO_6. (d), (e) Schematics of magnetic layers (*ab* planes) of 3*R*- (d) and 2*H*- (e) Na_2MnTeO_6.

III. RESULTS AND DISCUSSION

A. Crystal structure

A photograph of as-grown Na_2MnTeO_6 crystal is displayed in Fig. 1(a), left inset. The crystals are highly cleavable. The SEM image [Fig. 1(a), right inset] displays an atomically flat cleaved surface and terraces, features that are commonly observed in van der Waals materials. Thin flakes of these crystals are reddish and transparent in transmitted natural light, a characteristic of their optical band gap. As shown in Fig. 1(a), the powder x-ray diffraction (XRD) pattern of ground crystals can be fit well by a rhombohedral unit cell with $a = 5.219(1)$ Å and $c = 15.91(5)$ Å [Fig. 1(b)], but not the hexagonal unit cell reported for 2*H*-Na_2MnTeO_6 [Fig. 1(c)]. These results indicate that a polytype has been formed. A tiny crystal flake was selected for single-crystal x-ray-diffraction structure determination. The refinement result confirms the *R*-3 symmetry with an ABC-type stacking of disordered Mn-Te layers, which makes the material isostructural to a reported *R*-3 polytype of Na_2GeTeO_6 [15]. Introducing Mn-Te ordering creates two distinct sites in the honeycomb layer, increases the in-plane cell dimension, and lowers the lattice symmetry. Attempts to refine the crystal structure using such a model increased the R_1 value from 3.70 to 5.84%. If disorder is allowed in the model, the refinement gives occupancies Mn0.58Te0.42 in honeycomb site 1 and Mn0.42Te0.58 in honeycomb site 2. This result indicates that the Mn and Te in 3*R*-Na_2MnTeO_6 crystals are mostly statistically disordered [Fig. 1(d)], and that the lattice symmetry is closer to being centrosymmetric *R*-3. Therefore, an *R*-3 model with mixed Mn and Te in a ratio fixed to 0.5:0.5 was used to refine the single-crystal (SC)-XRD data. The reported Mn-Te disorder level is around 15% in 2*H*-Na_2MnTeO_6

TABLE I. Single-crystal structure refinement for $3R$-Na_2MnTeO_6 at 298(2) K.

Refined formula	Na_2MnTeO_6
Formula weight (F.W.) (g/mole)	313.62
Space group	R-3
Z	3
a(Å)	5.215(4)
c(Å)	15.94(2)
V(Å^3)	375.4(7)
Extinction coefficient	0.0028(10)
R_1	0.0360
ωR_2 [$I > 2\delta(I)$]	0.0702
Goodness of fit	1.147

[Fig. 1(e)] [16], which is much smaller than that observed in $3R$-Na_2MnTeO_6 as reported here. The powder XRD on crushed crystals shows sharp ($00L$) peaks without splitting in addition to K_{α_1} and K_{α_2}, which are consistent with the rhombohedral symmetry (Fig. S1) [21]. The crystallographic data for $3R$-Na_2MnTeO_6, including atomic positions, site occupancies, and refined thermal parameters, are listed in Tables I and II. The unit-cell parameters obtained from single-crystal diffraction match well with the ones obtained from the ground-crystal powder XRD. The crystal structure is registered with the Cambridge Structural Database, No. 2216668.

To further study our stacking polytype (especially the local symmetry), we examined thin lamellar samples cut from single-crystal $3R$-Na_2MnTeO_6 by scanning/transmission electron microscopy (S/TEM), as shown in Fig. 2. A low-magnification TEM image of a studied sample area is displayed in Fig. 2(a). The diffraction pattern in Fig. 2(b) verified that the polytype exhibits an R-3 structure which is consistent with the analysis from SC-XRD, with localized Mn-Te disordering. An atomic-resolution STEM image shown in Fig. 2(c) confirmed the $3R$ atomic stacking in the structure, viewed from the [110] direction. Note that Na atoms cannot be imaged in the STEM image due to their sensitivity to high-energy electron beam. The neighboring atomic spots display the same image contrast, which indicates a disordered distribution of Mn and Te. It should be mentioned that if Mn and Te atoms are orderly distributed in the structure, they will show clear image contrast because of the large difference in atomic number. In addition, stacking faults are observed in a few regions of the TEM lamellae. Figure S2(b) displays the STEM atomic imaging of an area with stacking faults [21], and the corresponding diffraction pattern shows satellite spots between some of the rhombohedral $00l$ diffraction peaks. The Mn and Te atoms are still disorderedly distributed in the stacking faults. Overall, both diffraction analysis and atomic-resolution imaging confirmed a disordered Mn-Te distribution in the single crystal, which is consistent with the single-crystal x-ray diffraction refinement result.

B. Magnetism

The magnetic susceptibility measured along the c and a directions under an applied field of 1000 Oe is displayed in Fig. 3(a). No long-range magnetic ordering is detected down to 1.8 K. The inset depicts the inverse susceptibility, for which a bending below 4 K along a reflects the onset of a short-range magnetic correlations. Curie-Weiss (CW) fitting gives $\theta_c =$ –3.0(4) K, $\mu_{\text{eff},c} = 4.0(5)\,\mu_B$, $\theta_{ab} =$ –4.1(7) K, and $\mu_{\text{eff},ab} =$ 3.9(9) μ_B per formula unit in the temperature range 7 to 20 K, and $\theta_c =$ –4.9(5) K, $\mu_{\text{eff},c} = 3.8(3)\,\mu_B$ per formula unit, $\theta_{ab} =$ –6.2(3) K, and $\mu_{\text{eff},ab} = 3.9(5)\,\mu_B$ per formula unit in the temperature range 100 to 150 K. The negative CW temperatures are an indication of dominant antiferromagnetic interactions both interlayer and intralayer. The magnetic susceptibility of polycrystalline sample is calculated by $\chi_{\text{poly}} = \frac{1}{3}\chi_c + \frac{2}{3}\chi_{ab}$. The CW fitting to that average gives $\theta_{\text{poly}} =$ –3.73(0) K, $\mu_{\text{eff,poly}} = 4.01(0)\,\mu_B$ per formula unit in the temperature range 7–20 K, and $\theta_{\text{poly}} =$ –9.2(3) K, $\mu_{\text{eff,poly}} =$ 3.8(5) μ_B per formula unit in the temperature range 200–300 K. The effective moments obtained from χ_{poly} are in good agreement with the expected spin-only value of 3.87 μB for the Mn^{4+} ($S = 3/2$) free ion. (The inverse susceptibility as a function of temperature curves for $H//c$, $H//a$, and calculated polycrystalline sample are plotted in Fig. S3 [21].) Figure 3(b) shows the isothermal magnetization versus field curve. Weak easy-axis anisotropy is observed, and no field-induced transitions are seen. In contrast, $2H$-Na_2MnTeO_6 is reported to have a long-range ordering transition at around 5.5 K that can be unhidden in the temperature-dependent susceptibility measured at high applied fields [16]. Similar measurements were performed on a $3R$-Na_2MnTeO_6 crystal along both the a and c directions (Fig. S4) [21], but the results do not show any sharp transitions in fields up to 9 T. As shown in Figs. S5(a) and S5(b) [21], the field-cooling and zero field-cooling susceptibility data measured at a field of 50 Oe do not show any detectable bifurcation, which rules out the possibilities of ferromagnetic moments or spin glassiness down to 1.8 K. The AC susceptibility was measured down to 1.8 K, and the results are shown in Figs. S5(c) and S5(d) [21]. The AC susceptibility χ'_{AC} does not show any anomaly or frequency dependence down to 1.8 K in zero DC field, while applying a 3-T field leads to a broad maximum at around 5 K in χ'_{AC}, implying that the material displays field-enhanced short-range magnetic ordering.

TABLE II. Atomic coordinates and equivalent isotropic displacement parameters from the single-crystal refinement of $3R$-Na_2MnTeO_6 at 298(2) K; space group R-3.

Atoms	Wyckoff site	x/a	y/b	z/c	Occupation	U_{eq}
Te	6c	2/3	1/3	0.495 54(9)	0.5	0.0093(5)
Mn	6c	2/3	1/3	0.495 54(9)	0.5	0.0093(5)
Na	6c	1/3	2/3	0.360 8(4)	1	0.0294(16)
O	18f	0.3814(12)	0.3884(11)	0.4310 (4)	1	0.0273(15)

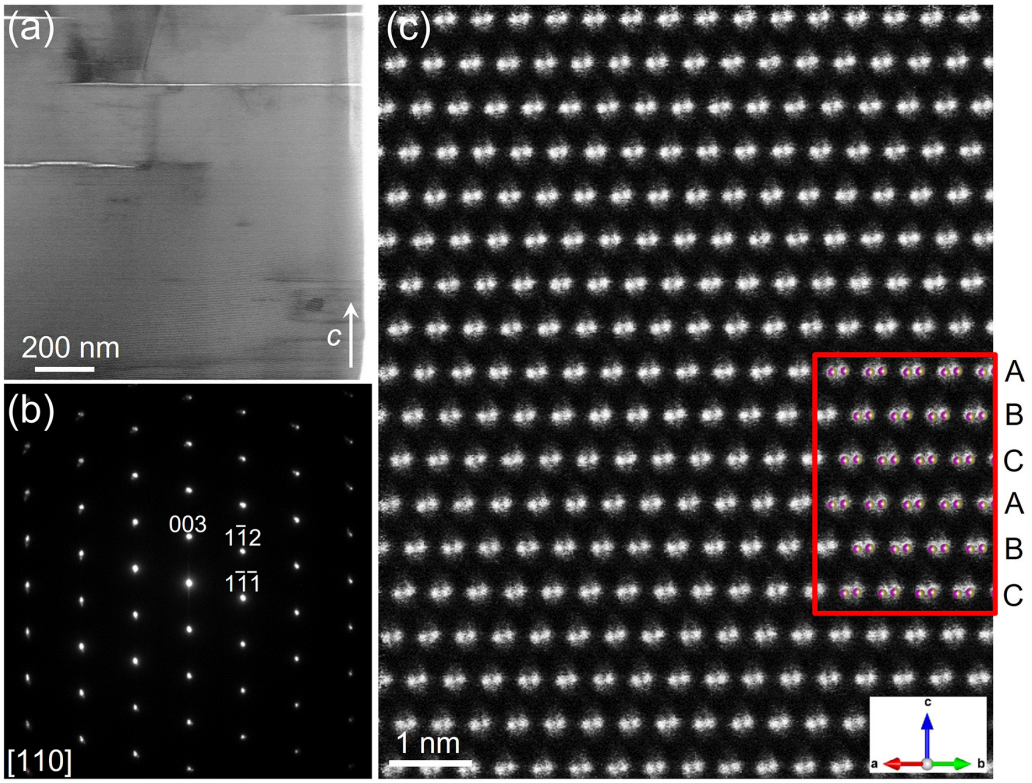

FIG. 2. (a), (b) Low-magnification TEM image and corresponding diffraction pattern. (c) STEM atomic image showing the Mn-Te atom arrays. The *R*-3 Mn-Te disordered structural model is superimposed on the region marked by the red square (Mn, purple; Te, yellow). All data are taken with electron beam parallel to the [110] direction.

C. Heat capacity

To further confirm the absence of long-range ordering and look for underlying quantum states, heat-capacity measurements were performed down to 0.5 K. Figure 4(a) displays the heat capacity of 3*R*-Na_2MnTeO_6 up to 170 K in zero field. The phonon contribution dominates in the high-temperature regime. However, it is found that the data cannot be well fitted by a Debye equation with one single Debye temperature. Therefore, a modified Debye equation, $C_{\text{phonon}} = 9R\sum_{n=1}^{2} C_n(\frac{T}{\Theta_{Dn}})^3 \int_0^{\Theta_{Dn}/T} \frac{x^4 e^x}{(e^x-1)^2} dx$, with two components is used to fit the heat-capacity data. The constraint is that $C_1 + C_2 = 10$, which is the total number of atoms in the chemical formula Na_2MnTeO_6. The fitting curve is displayed in red, and gives fitting parameters $C_1 = 4.75$, $\Theta_{D1} = 1196.1$ K, and $C_2 = 5.25$, $\Theta_{D2} = 349.6$ K. Note that the same two-component Debye equation has been applied to fit the high-temperature heat capacity of other oxide solids containing heavy tellurium atoms [22,23]. Below 30 K, a

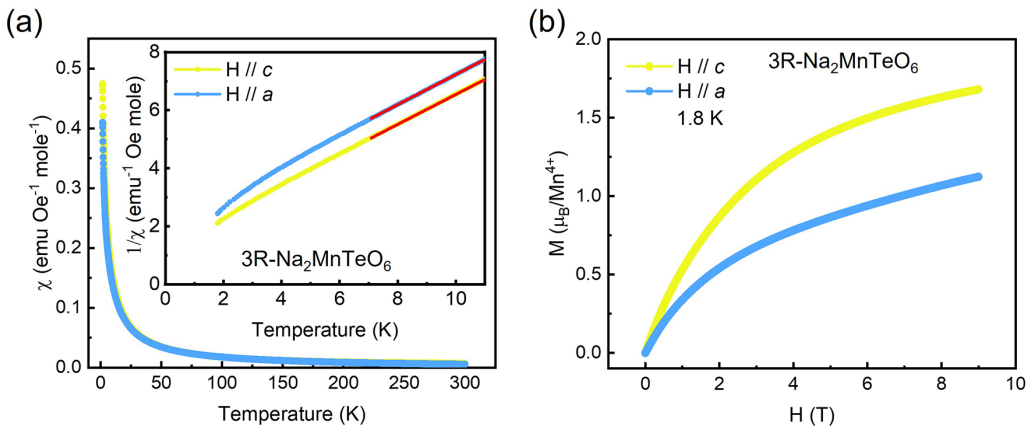

FIG. 3. (a) Magnetic susceptibility of 3*R*-Na_2MnTeO_6 vs temperature curves measured by 1000-Oe field along *c* and *a* are displayed in yellow and blue, respectively. Inset shows the low-temperature range inverse susceptibility and the CW fitting (red curves). See Fig. S3 for the high-temperature range [21]. (b) Isothermal magnetization vs magnetic field data at 1.8 K.

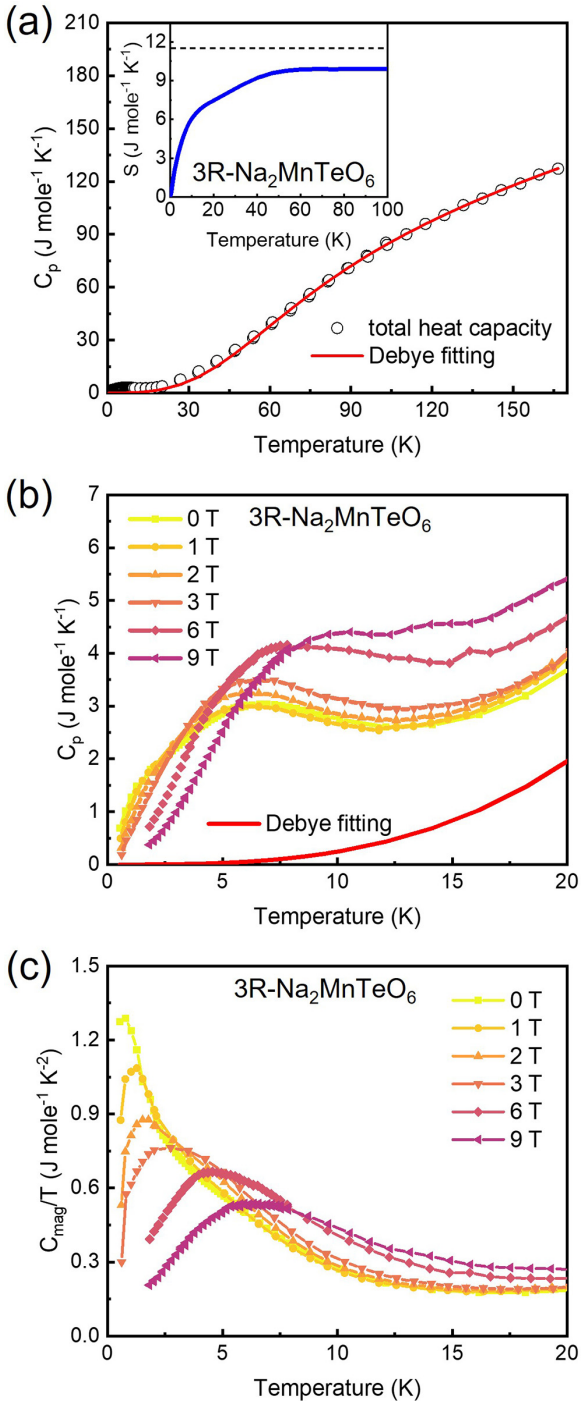

FIG. 4. (a) Black open circles show the heat capacity of $3R$-Na_2MnTeO_6 as a function of temperature. Red curve indicates the Debye fitting of the high-temperature range. Inset displays the magnetic entropy. (b), (c) Heat capacity and magnetic heat capacity over temperature measured at various fields applied along c axis.

broad peak with a maximum at around 5 K shows up and the heat capacity deviates from the phonon fitting, indicating the appearance of short-range magnetic correlations. After subtracting the phonon contribution, the magnetic entropy is obtained from integration and plotted in the inset of Fig. 4(a). The magnetic entropy saturates at around 60 K and reaches 9.57 J mole^{-1} K^{-1}. This value is 83% of the theoretical total magnetic entropy, 11.52 J mole^{-1} K^{-1} for $S = 3/2$ Mn^{4+}. The difference could be due to either an overestimated phonon contribution, or spin fluctuations at lower temperatures that lift the ground-state degeneracy [24]. As shown in Fig. 4(b), applying magnetic fields gradually shifts the broad peak to higher temperatures. Consistently, Fig. 4(c) shows that the peak in C_p/T, i.e., the major contribution of the magnetic entropy, can be shifted to higher temperatures by applying fields. This behavior has been commonly observed in frustrated magnets [25,26]. Note that even at zero field, the broad peak in C_p/T still exists, at a temperature of about 0.8 K. A comparison of the zero-field heat capacity of $3R$-Na_2MnTeO_6 and previously published $2H$-Na_2MnTeO_6 is displayed in Fig. S6 [21]. Obviously, $3R$-Na_2MnTeO_6 shows a much broader maximum than long-range ordered $2H$-Na_2MnTeO_6. We speculate that either different interlayer exchange interactions in the different stacking types or the Mn-Te disorder may account for the more disordered low-temperature spin state in $3R$-Na_2MnTeO_6 compared to that of $2H$-Na_2MnTeO_6.

IV. DISCUSSION

Previous work reports the presence of a very small amount of $3R$-Na_2MnTeO_6 for polycrystalline material synthesized at 600 °C–650 °C; but that the $3R$ phase irreversibly transforms to the $2H$ phase after heating at 700 °C–750 °C, indicating that the $3R$ phase is only stable at low temperature [17]. However, high temperature is critical for activating atom diffusion in the conventional solid-state reaction method, which may explain why single-phase $3R$-Na_2MnTeO_6 has not been synthesized previously. The single-crystal growth method reported in this work can overcome this issue and a pure $3R$ phase is finally obtained. To do that, the raw materials were first melted at 850 °C to ensure a uniform mixture, but the $3R$ phase did not immediately form. Instead, the phase forms crystals when the liquid is slowly cooled into the temperature range for which the $3R$ phase is thermodynamically most stable. Quenching the crucible at 650 °C results in tiny $3R$ crystals, which indicates that 650 °C is pretty close to the onset temperature of $3R$ crystallization. On the other hand, the relatively low crystallization temperature of $3R$ phase may count for the Mn-Te ionic disorder, possibly because ions do not have enough activation energy to order. Similar tendency that the low-temperature phase tends to show more chemical disorder has been observed in the $LiCoO_2$ system. In the cubic polymorph synthesized at a low temperature, the Li and Co ions exhibit site disorder [27–30], but in the high-temperature rhombohedral polymorph, the Li and Co ions fully order [31]. The Mn-Te disorder results in a centrosymmetric R-3 space-group crystal structure that is isostructural to the reported compound $3R$-Na_2GeTeO_6 which is also fully Ge-Te disordered [15]. In contrast, the analogous compound Li_2GeTeO_6 displays a 93% ordered Ge-Te distribution within a rhombohedral space group [32]. In some previously reported materials with a high-temperature order-disorder transition, nanodomains of ordered regions can be observed in a TEM [33]. However, though the electron diffraction patterns unveil some local ordered regions for the current material, no

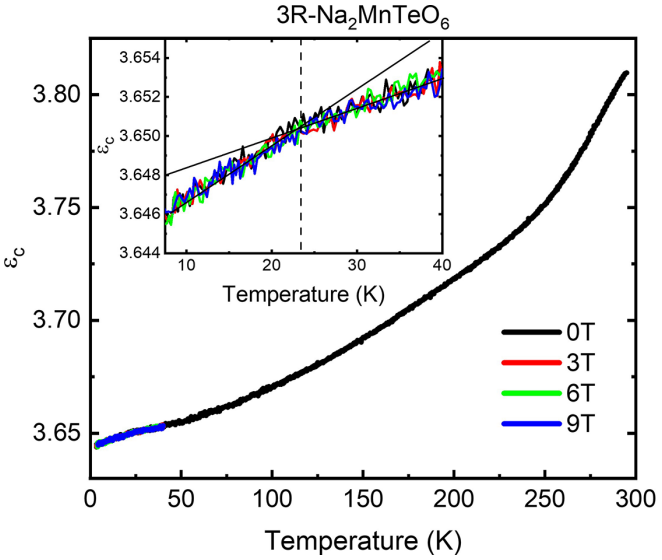

FIG. 5. Temperature-dependent dielectric permittivity of $3R$-Na_2MnTeO_6 along c axis (ε_c) measured with 44-kHz frequency and 1-V AC voltage, and at 0-, 3-, 6-, and 9-T magnetic field along c displayed by the black, red, green, and blue curves, respectively.

domain features are observed in the real-space TEM images of $3R$-Na_2MnTeO_6, which suggests that a high-temperature order-disorder transition does not happen in this case.

Single-ion anisotropy and spin degeneracy play central roles in determining the low-temperature ground states of frustrated magnets. Quantum fluctuations are typically most significant in systems with $S = 1/2$, leading to a highly entangled quantum spin-liquid state [34]. As a special case, Co^{2+} has spin 3/2, but the participation of spin-orbit coupling and crystal electric field can generate an effective doublet spin at low temperature [35–38]. In Cr^{3+}, Mn^{4+}, and Fe^{3+} systems with larger spin values, geometrically frustrated antiferromagnetic interactions may also lead to spin disordered states. Examples include $MgCr_2O_4$ ($S = 3/2$ for Cr^{3+}) [39], $BaTi_{1/2}Mn_{1/2}O_3$ ($S = 3/2$ for Mn^{4+}) [40], and $Li_9Fe_3(P_2O_7)_3(PO_4)_2$ ($S = 5/2$ for Fe^{3+}) [41]. In $3R$-Na_2MnTeO_6, the Mn ion has a formal valence of $+4$ and $S = 3/2$. The effective magnetic moment obtained from magnetic data in all temperature ranges is very close to that value (See Sec. III B), which suggests the orbital contribution to the effective moment is negligible.

As shown in Fig. 5, the dielectric permittivity of $3R$-Na_2MnTeO_6 shows a subtle anomaly at ~23 K, marked by the dashed line. An applied magnetic field does not affect this feature at all, either out of plane or in plane (similar, not shown), implying that this transition is not induced by the coupling of crystal structure and short-range magnetic correlations, but instead is purely structural. Note that the anomaly at around 250 K is likely from a dipole freezing and may not be intrinsic. In another sodium-containing layered tellurate $Na_2Ni_2TeO_6$, it was found that the intralayer diffusion of Na ions could create Na-ordering patterns and further lower the lattice symmetry [42], which provides a possible scenario for a structural transition in $3R$-Na_2MnTeO_6. Note that no clear anomalies are observed in the magnetic susceptibility or heat capacity versus temperature data at 23 K, suggesting that the change of structure across this transition is subtle, such as slight displacements of the Na positions. In addition, though the room-temperature space group R-3 is centrosymmetric, all the mirror symmetries are broken, and ferrorotation order [43] is a possibility. The single crystals obtained here therefore provide excellent platforms for future studies concerning ferrorotation and ferrorotational-domain configurations using optical techniques such as second-harmonic generation [44].

V. CONCLUSION

Crystals of $3R$-Na_2MnTeO_6 were synthesized using a flux method and their properties are reported. Structure analysis by x-ray- and electron diffraction reveals an R-3 space group and ABC-type stacking crystal structure, i.e., a different $3R$ stacking polytype compared to a reported $2H$ phase. Magnetic- and heat-capacity measurements are characteristic of low-temperature short-range spin correlations and the absence of long-range spin order down to 0.5 K. Our study reflects the fact that the stacking of a layered oxide can be determined by varying the synthesis method. Our results also demonstrate a spin-disordered state in a low-dimensional honeycomb lattice at low temperature. Considering the non-negligible level of Mn-Te chemical disorder, it cannot be concluded whether the different magnetism of $2H$- and $3R$-Na_2MnTeO_6 is dominated by stacking types or chemical disorder. Therefore, future research should focus on how to diminish the chemical disorder by optimizing the flux-growth condition such as a slower cooling rate or a careful annealing of the as-grown crystals. In addition, inspired by the fact that $3R$-Li_2GeTeO_6 shows much better Ge-Te ordering than $3R$-Na_2GeTeO_6, introducing Li in $3R$-Na_2MnTeO_6, i.e., $3R$-$Li_xNa_{2-x}MnTeO_6$, may help Mn and Te ions to order. The growth of $3R$-Na_2MnTeO_6 single crystal brings up opportunities such as searching for a magnetic excitation continuum, exotic local structures formed by interlayer ions, and studies of structural ferroic order by advanced optical techniques, and may initiate further exploration of the stacking polytypes of layered oxides.

ACKNOWLEDGMENTS

This research was primarily supported by the Gordon and Betty Moore Foundation, Grant No. GBMF-9066. The authors acknowledge the use of Princeton's Imaging and Analysis Center (IAC), which is partially supported by the Princeton Center for Complex Materials (PCCM), a National Science Foundation (NSF) Materials Research Science and Engineering Center (MRSEC; Grant No. DMR-2011750). The single-crystal diffraction data were obtained in a laboratory at Rutgers University, supported by the U.S. DOE-BES under Contract No. DE SC0022156.

[1] N. D. Mermin and H. Wagner, Absence of Ferromagnetism or Antiferromagnetism in One- or Two-Dimensional Isotropic Heisenberg Models, Phys. Rev. Lett. **17**, 1133 (1966).

[2] L. Balents, Spin liquids in frustrated magnets, Nature (London) **464**, 199 (2010).

[3] C. Broholm, R. J. Cava, S. A. Kivelson, D. G. Nocera, M. R. Norman, and T. Senthil, Quantum spin liquids, Science **367**, eaay0668 (2020).

[4] S. H. Lee, H. Kikuchi, Y. Qiu, B. Lake, Q. Huang, K. Habicht, and K. Kiefer, Quantum-spin-liquid states in the two-dimensional kagome antiferromagnets $ZnxCu_{4-x}(OD)6Cl_2$, Nat. Mater. **6**, 853 (2007).

[5] Y. Shirata, H. Tanaka, A. Matsuo, and K. Kindo, Experimental Realization of a Spin-1/2 Triangular-Lattice Heisenberg Antiferromagnet, Phys. Rev. Lett. **108**, 057205 (2012).

[6] J. J. Wen, S. M. Koohpayeh, K. A. Ross, B. A. Trump, T. M. McQueen, K. Kimura, S. Nakatsuji, Y. Qiu, D. M. Pajerowski, J. R. D. Copley, and C. L. Broholm, Disordered Route to the Coulomb Quantum Spin Liquid: Random Transverse Fields on Spin Ice in $Pr_2Zr_2O_7$, Phys. Rev. Lett. **118**, 107206 (2017).

[7] T. Furukawa, K. Miyagawa, T. Itou, M. Ito, H. Taniguchi, M. Saito, S. Iguchi, T. Sasaki, and K. Kanoda, Quantum Spin Liquid Emerging from Antiferromagnetic Order by Introducing Disorder, Phys. Rev. Lett. **115**, 077001 (2015).

[8] X. Xu, F.-T. Huang, A. S. Admasu, J. Kim, K. Wang, E. Feng, H. Cao, and S.-W. Cheong, Bilayer square lattice $Tb_2SrAl_2O_7$ with structural Z_8 vortices and magnetic frustration, Chem. Mater. **34**, 1225 (2022).

[9] J. A. Wilson and A. D. Yoffe, The transition metal dichalcogenides discussion and interpretation of the observed optical, electrical and structural properties, Adv. Phys. **18**, 193 (1969).

[10] H. Luo, W. Xie, J. Tao, H. Inoue, A. Gyenis, J. W. Krizan, A. Yazdani, Y. Zhu, and R. J. Cava, Polytypism, polymorphism, and superconductivity in $TaSe_{2-x}Te_x$, Proc. Natl. Acad. Sci. **112**, E1174 (2015).

[11] T. A. Empante, Y. Zhou, V. Klee, A. E. Nguyen, I. H. Lu, M. D. Valentin, S. A. Naghibi Alvillar, E. Preciado, A. J. Berges, C. S. Merida, M. Gomez, S. Bobek, M. Isarraraz, E. J. Reed, and L. Bartels, Chemical vapor deposition growth of few-layer $MoTe_2$ in the $2H$, $1T'$, and 1T phases: Tunable properties of $MoTe_2$ films, ACS Nano **11**, 900 (2017).

[12] X. Mi, X. Wang, H. Gui, M. Pi, T. Zheng, K. Yang, Y. Gan, P. Wang, A. Li, A. Wang, L. Zhang, Y. Su, Y. Chai, and M. He, Stacking faults in α-$RuCl_3$ revealed by local electric polarization, Phys. Rev. B **103**, 174413 (2021).

[13] H. Zhou, T. Xie, T. Taniguchi, K. Watanabe, and A. F. Young, Superconductivity in rhombohedral trilayer graphene, Nature (London) **598**, 434 (2021).

[14] E. A. Zvereva, G. V. Raganyan, T. M. Vasilchikova, V. B. Nalbandyan, D. A. Gafurov, E. L. Vavilova, K. V. Zakharov, H. J. Koo, V. Y. Pomjakushin, A. E. Susloparova, A. I. Kurbakov, A. N. Vasiliev, and M. H. Whangbo, Hidden magnetic order in the triangular-lattice magnet Li_2MnTeO_6, Phys. Rev. B **102**, 094433 (2020).

[15] P. M. Woodward, A. W. Sleight, L.-S. Du, and C. P. Grey, Structural studies and order–disorder phenomenon in a series of new quaternary tellurates of the type $A^{2+}\,M^{4+}\,Te^{6+}\,O_6$ and $A^{1+}{}_2\,M^{4+}\,Te^{6+}\,O_6$, J. Solid State Chem. **147**, 99 (1999).

[16] A. I. Kurbakov, A. E. Susloparova, V. Y. Pomjakushin, Y. Skourski, E. L. Vavilova, T. M. Vasilchikova, G. V. Raganyan, and A. N. Vasiliev, Commensurate helicoidal order in the triangular layered magnet Na_2MnTeO_6, Phys. Rev. B **105**, 064416 (2022).

[17] V. B. Nalbandyan, I. L. Shukaev, G. V. Raganyan, A. Svyazhin, A. N. Vasiliev, and E. A. Zvereva, Preparation, crystal chemistry, and hidden magnetic order in the family of trigonal layered tellurates $A_2Mn(4+)TeO_6$ (A = Li, Na, Ag, or Tl), Inorg. Chem. **58**, 5524 (2019).

[18] D. Wang, Y. Zhang, Q. Liu, B. Zhang, D. Yang, and Y. Wang, Band gap modulation and nonlinear optical properties of quaternary tellurates Li_2GeTeO_6, Dalton Trans. **51**, 8955 (2022).

[19] G. M. Sheldrick, Crystal structure refinement with SHELXL, Acta Crystallogr. Sect. C: Struct Chem. **71**, 3 (2015).

[20] G. M. Sheldrick, SHELXT–Integrated space-group and crystal-structure determination, Acta Crystallogr. Sect. A: Found. Adv. **71**, 3 (2015).

[21] See Supplemental Material at http://link.aps.org/supplemental/10.1103/PhysRevMaterials.7.024407 for $(00L)$ peaks in XRD, STEM on stacking-fault area, inverse susceptibility, M/H, AC susceptibility, and comparison of heat capacity between $2H$ and $3R$ phases.

[22] L. Ortega-San Martin, J. P. Chapman, L. Lezama, J. Sánchez Marcos, J. Rodríguez-Fernández, M. I. Arriortua, and T. Rojo, Magnetic properties of the ordered double perovskite Sr_2MnTeO_6, Eur. J. Inorg. Chem. **2006**, 1362 (2006).

[23] L. Li, X. Hu, Z. Liu, J. Yu, B. Cheng, S. Deng, L. He, K. Cao, D.-X. Yao, and M. Wang, Structure and magnetic properties of the $S = 3/2$ zigzag spin chain antiferromagnet $BaCoTe_2O_7$, Sci. China Phys. Mech. Astron. **64**, 287412 (2021).

[24] R. Zhong, M. Chung, T. Kong, L. T. Nguyen, S. Lei, and R. J. Cava, Field-induced spin-liquid-like state in a magnetic honeycomb lattice, Phys. Rev. B **98**, 220407 (2018).

[25] S. H. Baek, S. H. Do, K. Y. Choi, Y. S. Kwon, A. U. B. Wolter, S. Nishimoto, J. van den Brink, and B. Büchner, Evidence for a Field-Induced Quantum Spin Liquid in α-$RuCl_3$, Phys. Rev. Lett. **119**, 037201 (2017).

[26] B. Gao, T. Chen, D. W. Tam, C.-L. Huang, K. Sasmal, D. T. Adroja, F. Ye, H. Cao, G. Sala, M. B. Stone, C. Baines, J. A. T. Verezhak, H. Hu, J.-H. Chung, X. Xu, S.-W. Cheong, M. Nallaiyan, S. Spagna, M. B. Maple, A. H. Nevidomskyy, E. Morosan, G. Chen, and P. Dai, Experimental signatures of a three-dimensional quantum spin liquid in effective spin-1/2 $Ce_2Zr_2O_7$ pyrochlore, Nat. Phys. **15**, 1052 (2019).

[27] R. Gummow, M. Thackeray, W. David, and S. Hull, Structure and electrochemistry of lithium cobalt oxide synthesised at 400 °C, Mater. Res. Bull. **27**, 327 (1992).

[28] E. Rossen, J. Reimers, and J. Dahn, Synthesis and electrochemistry of spinel LT $LiCoO_2$, Solid State Ionics **62**, 53 (1993).

[29] H. Wang, Y. I. Jang, B. Huang, D. R. Sadoway, and Y. M. Chiang, TEM study of electrochemical cycling-induced damage and disorder in $LiCoO_2$ cathodes for rechargeable lithium batteries, J. Electrochem. Soc. **146**, 473 (1999).

[30] T. Tsuruhama, T. Hitosugi, H. Oki, Y. Hirose, and T. Hasegawa, Preparation of layered-rhombohedral $LiCoO_2$ epitaxial thin films using pulsed laser deposition, Appl. Phys. Express **2**, 085502 (2009).

[31] Y. Takahashi, N. Kijima, K. Dokko, M. Nishizawa, I. Uchida, and J. Akimoto, Structure and electron density analysis of electrochemically and chemically delithiated $LiCoO_2$ single crystals, J. Solid State Chem. **180**, 313 (2007).

[32] M.-H. Zhao, W. Wang, Y. Han, X. Xu, Z. Sheng, Y. Wang, M. Wu, C. P. Grams, J. Hemberger, D. Walker, M. Greenblatt, and M.-R. Li, Reversible structural transformation between polar polymorphs of Li_2GeTeO_6, Inorg. Chem. **58**, 1599 (2019).

[33] X. Xu, F.-T. Huang, A. S. Admasu, M. Kratochvílová, M.-W. Chu, J.-G. Park, and S.-W. Cheong, Multiple ferroic orders and toroidal magnetoelectricity in the chiral magnet $BaCoSiO_4$, Phys. Rev. B **105**, 184407 (2022).

[34] A. Kitaev, Anyons in an exactly solved model and beyond, Ann. Phys. **321**, 2 (2006).

[35] R. Zhong, S. Guo, G. Xu, Z. Xu, and R. J. Cava, Strong quantum fluctuations in a quantum spin liquid candidate with a Co-based triangular lattice, Proc. Natl. Acad. Sci. **116**, 14505 (2019).

[36] R. Zhong, T. Gao, N. P. Ong, and R. J. Cava, Weak-field induced nonmagnetic state in a Co-based honeycomb, Sci. Adv. **6**, eaay6953 (2020).

[37] W. Yao and Y. Li, Ferrimagnetism and anisotropic phase tunability by magnetic fields in $Na_2Co_2TeO_6$, Phys. Rev. B **101**, 085120 (2020).

[38] G. Lin, J. Jeong, C. Kim, Y. Wang, Q. Huang, T. Masuda, S. Asai, S. Itoh, G. Günther, M. Russina, Z. Lu, J. Sheng, L. Wang, J. Wang, G. Wang, Q. Ren, C. Xi, W. Tong, L. Ling, Z. Liu, L. Wu, J. Mei, Z. Qu, H. Zhou, X. Wang, J.-G. Park, Y. Wan, and J. Ma, Field-induced quantum spin disordered state in spin-1/2 honeycomb magnet $Na_2Co_2TeO_6$, Nat. Commun. **12**, 5559 (2021).

[39] X. Bai, J. A. M. Paddison, E. Kapit, S. M. Koohpayeh, J. J. Wen, S. E. Dutton, A. T. Savici, A. I. Kolesnikov, G. E. Granroth, C. L. Broholm, J. T. Chalker, and M. Mourigal, Magnetic Excitations of the Classical Spin Liquid $MgCr_2O_4$, Phys. Rev. Lett. **122**, 097201 (2019).

[40] F. A. Garcia, U. F. Kaneko, E. Granado, J. Sichelschmidt, M. Hölzel, J. G. S. Duque, C. A. J. Nunes, R. P. Amaral, P. Marques-Ferreira, and R. Lora-Serrano, Magnetic dimers and trimers in the disordered $S = 3/2$ spin system $BaTi_{1/2}Mn_{1/2}O_3$, Phys. Rev. B **91**, 224416 (2015).

[41] E. Kermarrec, R. Kumar, G. Bernard, R. Hénaff, P. Mendels, F. Bert, P. L. Paulose, B. K. Hazra, and B. Koteswararao, Classical Spin Liquid State in the $S = 5/2$ Heisenberg Kagome Antiferromagnet $Li_9Fe_3(P_2O_7)_3(PO_4)_2$, Phys. Rev. Lett. **127**, 157202 (2021).

[42] S. K. Karna, Y. Zhao, R. Sankar, M. Avdeev, P. C. Tseng, C. W. Wang, G. J. Shu, K. Matan, G. Y. Guo, and F. C. Chou, Sodium layer chiral distribution and spin structure of $Na_2Ni_2TeO_6$ with a Ni honeycomb lattice, Phys. Rev. B **95**, 104408 (2017).

[43] S.-W. Cheong, D. Talbayev, V. Kiryukhin, and A. Saxena, Broken symmetries, non-reciprocity, and multiferroicity, npj Quantum Mater. **3**, 19 (2018).

[44] W. Jin, E. Drueke, S. Li, A. Admasu, R. Owen, M. Day, K. Sun, S.-W. Cheong, and L. Zhao, Observation of a ferro-rotational order coupled with second-order nonlinear optical fields, Nat. Phys. **16**, 42 (2020).